Peer reviewed version

University of Bristol - Explore Bristol Research
General rights

MAINSHOCK-AFTERSHOCK STATE-DEPENDENT FRAGILITY CURVES: A CASE OF WOOD-FRAME HOUSES IN BRITISH COLUMBIA, CANADA

Lizhong Zhang[1], Katsuichiro Goda[2,3], Flavia De Luca[1], and Raffaele De Risi[1]

[1]Department of Civil Engineering, University of Bristol, Bristol, United Kingdom
[2]Department of Earth Sciences, University of Western Ontario, London, Canada
[3]Department of Statistical & Actuarial Sciences, University of Western Ontario, London, Canada

During a mainshock-aftershock (MSAS) sequence, there is no time to retrofit structures that are damaged by a mainshock, therefore, aftershocks could cause additional damage. This study proposes a new approach to develop state-dependent fragility curves using real MSAS records. Specifically, structural responses before and after each event of MSAS sequences are used to obtain statistical relationships among the engineering demand parameter prior to the seismic event (*pre-EDP*), the intensity measure of the seismic event (*IM*), and the engineering demand parameter after the seismic event (*post-EDP*). The developed fragility curves account for damage accumulation, providing the exceeding probability of damage state (DS) given the *IM* of the event and the DS of the structure prior to the seismic excitation. The UBC-SAWS model, which was developed for wood-frame houses in British Columbia, Canada, is considered as a case study application. Results indicate that, for the examined structural typology, state-dependent fragility curves based on residual inter-storey drift ratio (*pre-EDP*), peak ground velocity (*IM*), and maximum inter-storey drift ratio (*post-EDP*) are the best choice to characterise the cumulative damage effect. An illustration of the developed fragility curves is provided by considering a hypothetical MSAS scenario of a M_w 9.0 Cascadia mainshock triggering a M_w 6.0 crustal event in the Leech River fault, affecting wooden houses in Victoria, Canada. The MSAS scenario increases Yellow tags (restricted access) by 12.3% and Red tags (no access) by 4.8%.

KEYWORDS

State-dependent aftershock fragility curves, real mainshock-aftershock sequences, nonlinear dynamic analysis of wood-frame houses, cloud analysis, multinomial distribution

1 INTRODUCTION

Recent M_w 9.0 earthquake sequences, such as the 2011 Tohoku earthquake sequence, showed the destructive effects of aftershocks on buildings [1,2]. Cumulative damage due to aftershocks can have a significant impact on the post-earthquake risk assessment immediately after a mainshock, for example, building tagging, inspection prioritisation, re-occupancy decision, and retrofitting [3–7]. Similar destructive mainshock-aftershock (MSAS) sequences could occur in other subduction zone regions. For instance, based on turbidite records in the past 10,000 years, the Cascadia subduction zone (CSZ) from Vancouver Island to Northern California ruptured 19 times with M_w 9.0-class earthquakes [8], resulting in an average recurrence period of 526 years. To account for the cumulative damage of MSAS sequences, a fragility model that can estimate the DS of a structure after each event during an earthquake sequence is necessary.

Many studies have focused on the cumulative damage effects of aftershocks on different types of structures [9–12]. Among these, Luco *et al.* (2004) developed a set of state-dependent fragility curves by using non-linear dynamic analysis. A steel moment-resisting frame model was subjected to scaled mainshock records to attain different levels of damage (referred as pre-DSs, i.e., the damage registered as a result of the mainshock). Following that, aftershock records (which were identical to the mainshock record set) were applied to the mainshock-damaged building by performing incremental dynamic analysis (IDA) attaining cumulative damage resulting from the sequence (referred as post-DSs, i.e., the damage on the structure subjected to the aftershocks). This is so-called back-to-back application of mainshock records [10]. The cumulative damage effects due to aftershocks were captured by the damage accumulation from the pre-DS (characterised by *pre-EDP*) to the post-DS (characterised by *post-EDP*). Raghunandan *et al.* (2015) extended Luco *et al.*'s approach to a reinforced concrete building by modelling it as a nonlinear multi-degree-of-freedom system and used the maximum inter-storey drift ratio (MaxISDR) as *EDP*. Ebrahimian *et al.* (2014) developed a performance-based framework for aftershock risk forecasting which consists of an epidemic-type aftershock sequence model and event-based aftershock fragility curves [7]. The ground motion records that were constructed for developing event-dependent aftershock fragility curves were selected from the pool of observed aftershock events.

The procedure by Luco *et al.* (2004) facilitates various post-earthquake decision-making, such as building-tagging and seismic loss estimation. However, there are four aspects that can be improved. (1) Since the aftershock

57 records from the back-to-back application are constructed from mainshock records, the link between the pre-structural
58 response by the mainshock and the post-structural response by the aftershock is eliminated. Thus, real MSAS records
59 are desirable. (2) The *post-EDP* may be overestimated, when the back-to-back application of mainshock records is
60 used for aftershock records with IDA [13]. (3) The computational cost of the back-to-back approach with IDA is high
61 [12]. (4) An appropriate set of *IMs* and *EDPs* needs to be selected to represent the intensity of ground motions and
62 structural responses, respectively. The spectral acceleration (Sa) at the fundamental period of a structure is widely
63 used as *IM* [14–16]. However, using a single-period Sa may not be effective, because higher mode effects and period
64 elongation of the structure are also important [17], and a sufficient *IM* would allow to amplify records with moderate
65 scaling factors to have more data points without causing significant biases [18]. Therefore, other *IMs*, such as Arias
66 intensity (AI), cumulative absolute velocity (CAV), spectral intensity (SI), and peak ground velocity (PGV), should
67 be taken into consideration in identifying the most suitable *IM* for the development of state-dependent aftershock
68 fragility curves.
69   This study develops a new approach to produce the state-dependent fragility curves due to real MSAS
70 sequences, which can be implemented to perform short-term post-earthquake risk assessments in major subduction
71 zones. The novelties of this study are that (1) a large set of real MSAS sequences with wide ranges of rupture distances
72 (0-270 km) and magnitudes (5.0-9.0) is used for the fragility assessment. (2) Rather than attaining each pre-DS with
73 scaled mainshock records [10], structural responses before and after each event due to the real MSAS sequences with
74 moderate scaling factors are used to obtain *pre-EDP – IM – post-EDP* sets for the development of state-dependent
75 fragility curves. (3) To reduce the computational cost from the back-to-back approach, a new approach that adopts
76 cloud analysis [19] with moderate scaling factors to scale the entire real MSAS sequences is proposed to develop the
77 state-dependent fragility curves. The 3D dataset (*pre-EDP – IM – post-EDP*) is binned according to the same pre-DS.
78 For each *IM – post-EDP* dataset that is classified by the same pre-DS, *IM* values corresponding to specific *post-EDP*
79 intervals are then fitted using the lognormal distribution and multinomial distribution [20,21] to produce the state-
80 dependent fragility curves. (4) Different combinations of *IMs* and *EDPs* are evaluated in developing state-dependent
81 seismic fragility curves given the *pre-EDP – IM – post-EDP* sets from the real MSAS sequences.
82   The procedure of developing state-dependent fragility curves for MSAS sequences is applied to wooden
83 houses in British Colombia, Canada that are represented by the UBC-SAWS (seismic analysis of wood-frame
84 structure) models. The wood-frame house is selected, because 56% of buildings in British Columbia are wood-frame
85 houses, 40% of which were built before 1970 [22]. Since seismic provisions of the National Building Code of Canada
86 were adopted and enforced in British Columbia after 1973, the majority of old residential houses can be considered
87 as 'non-engineered' from seismic design viewpoints. Consequently, many wood-frame houses with low seismic
88 resistances may suffer significant damage due to a M_w 9.0 mainshock and aftershocks in the CSZ.
89   This paper is organised as follows. A general description of the new approach to develop the state-dependent
90 fragility curves is given in Section 2. To demonstrate the new approach, the input ground motion records and UBC-
91 SAWS model are also described in Section 2. After identifying the appropriate *EDP* and *IM* for the SAWS model in
92 Section 3, Section 4 implements the new approach to develop the state-dependent fragility curves and presents the
93 results of deriving such fragility curves for the wood-frame houses in British Columbia, Canada.
94
95 **2 METHODOLOGY**
96
97 **2.1   Procedures to develop the state-dependent fragility curves**
98 A general procedure to develop the state-dependent fragility curves is illustrated below:
99   •   Real records of subduction-crustal MSAS sequences from local or global record datasets at the target site are
100   gathered. Such MSAS can later be used as real or scaled records with moderate scaling factor values;
101   •   Non-linear structural dynamic analyses of a target building model using the MSAS sequences are performed;
102   •   Structural responses before and after each event and the intensity measure of each event during a sequence
103   are recorded and used to develop statistical *pre-EDP – IM – post-EDP* relationships;
104   •   The efficiency and sufficiency of the *IM* associated with the *post-EDP* are examined. This allows using
105   moderate scaling factors for cloud analysis to reduce the high computational cost from IDA;
106   •   Since *EDPs* can be associated with the DS of the structure, before developing the state-dependent fragility
107   curves, the pre-DS and post-DS associated with *pre-EDP* and *post-EDP* are defined.
108   •   Finally, the 3D dataset (*pre-EDP – IM – post-EDP*) is binned according to the same pre-DS; for each bin, *IM*
109   values corresponding to specific post-DSs are then fitted progressively using different functional forms (e.g.,
110   lognormal and multinomial functions) to produce the fragility curves.

111   To illustrate the key concept of cumulative damage due to repeated earthquakes and the potential application
112 of state-dependent fragility, a schematic diagram of cumulative damage by multiple events is shown in **Figure 1**
113 [10,23]. The residual capacity of the structure may be decreased as more events affect the structure. For instance, for
114 the first shock, the structure starts from an undamaged condition, and therefore, given IM_1 of the first event only, the
115 post-DS after the first event can be estimated. More in general, with IM_j of the j-th shock and pre-DS_i before the j-th
116 shock, the post-DS_i can be evaluated, and this procedure can be applied recursively.
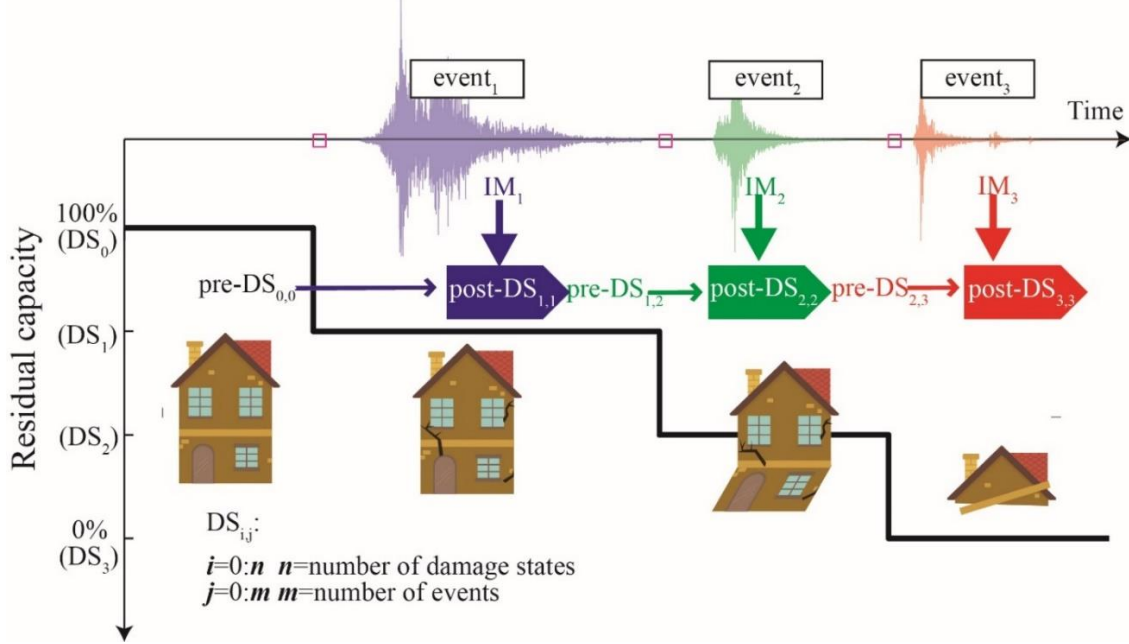

117
118   **Figure 1. Illustration of damage accumulation due to a mainshock-aftershock sequence.**
119

120 **2.2   Mainshock-aftershock ground motion records**
121 Using appropriate ground motion records to represent real MSAS sequences is important for seismic demand
122 estimation. The real MSAS record datasets from [24] and [25] are described in this section, which consist of 596
123 MSAS sequences of real earthquakes. The magnitude-distance plots of the 596 mainshocks (with filled markers) and
124 1,685 aftershocks (with unfilled markers) are shown in **Figure 2** by distinguishing between the PEER-NGA database,
125 in which only crustal records are provided, and Japanese K/KiK/SK-net database, where all crustal, in-slab and
126 interface records are available. Crustal earthquakes from the NGA and K/KiK/SK-net databases have lower
127 magnitudes and shorter distances than the interface and in-slab events from the K/KiK/SK-net database. The 596
128 records from this study have a magnitude range of 5.0-9.0 from different types of events, and include the 2011 M_w 9.0
129 Tohoku sequences with rupture distances up to 270 km. There are 2,281 events (202 crustal NGA events, 374 crustal-
130 K/KiK/SK events, 1,538 interface events, and 167 in-slab events) from 596 sequences × 2 horizontal components,
131 thus 4,562 *pre-EDP – IM – post-EDP* triplets (1,192 mainshocks and 3,370 aftershocks) can be obtained.
132   The design spectrum with site class C in Victoria [26] and response spectra with median and 16th/84th
133 percentiles of mainshocks and aftershocks are shown in **Figure 3(a)**. Because some large subduction earthquake
134 records (e.g., the 2011 Tohoku event with M_w 9.0) were recorded hundreds of kilometres away from the record stations,
135 the response spectra of the mainshocks is not strong in comparison with the design spectrum. The response spectra of
136 the mainshocks are generally higher than those of the aftershocks. Such inherent characteristics of natural records
137 should be automatically incorporated in developing state-dependent seismic fragility curves using the above defined
138 sets of MSAS series. **Figure 3**(b) shows the response spectra of median and 16th/84th percentiles of all earthquake
139 types without distinction between mainshocks and aftershocks.
140   Since the median response spectra of the aftershocks are smaller than the mainshocks, scaling factors are
141 necessary to ensure that the structure reaches collapse state for the development of fragility curves. Unlike other IDA
142 studies [19,27] that performed detailed record selection (e.g., CMS) and allowed high scaling factors up to 10, this
143 study uses cloud analysis [28] and applies moderate scaling factors to the entire MSAS sequences. Vamvatsikos and
144 Cornell (2002) indicated that the sufficiency of *IM* is important to allow a high scaling factor for record scaling. In
145 this study by selecting the sufficient and efficient *IM* and the most suitable *EDP* from Section 3, moderate scaling
146 factors of up to 5 are considered to be acceptable for cloud analysis, as suggested by other studies [19,29].
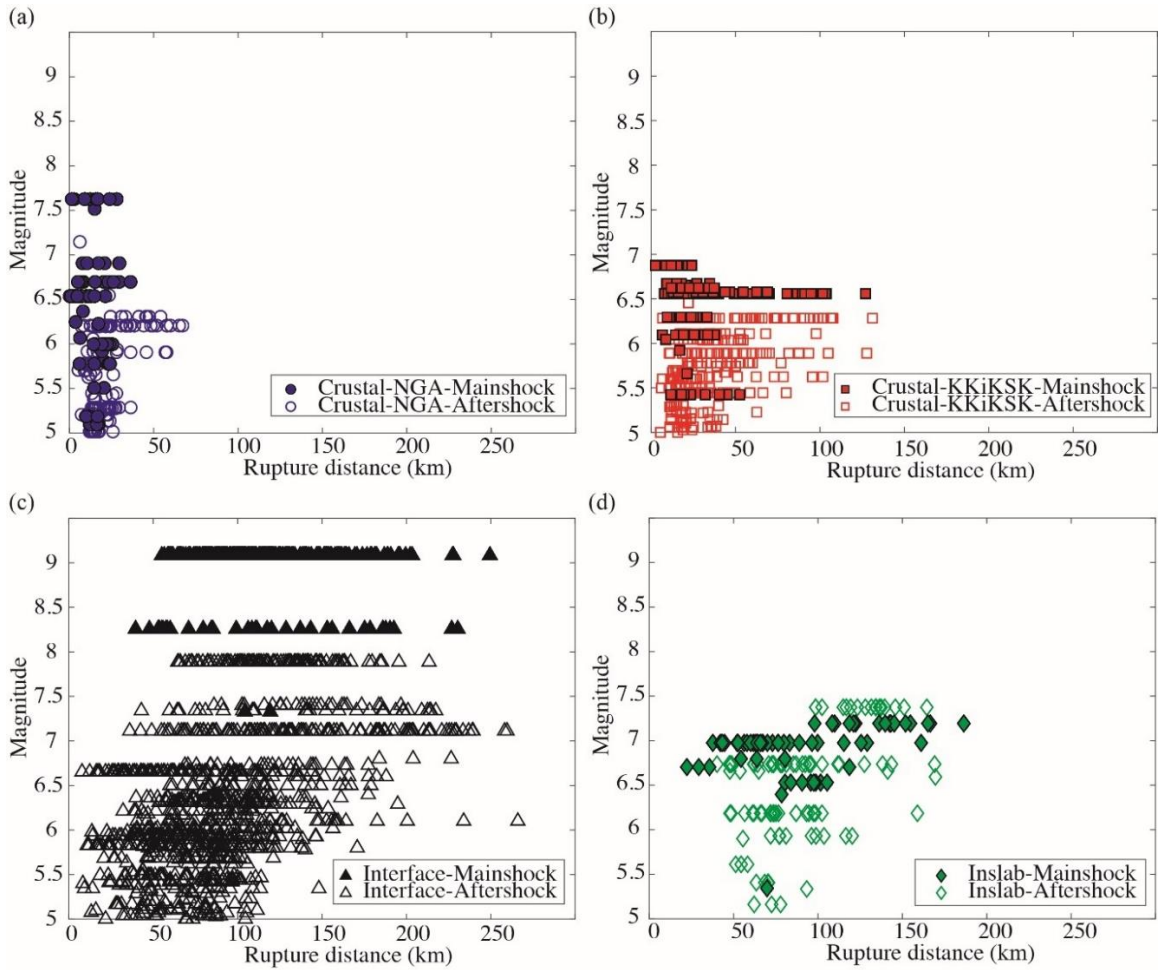
147
148   **Figure 2. Magnitude-distance plot of the mainshocks (with filled markers) and aftershocks (with unfilled**
149   **markers) including (a) crustal-NGA, (b) crustal-K/KiK/SK, (c) interface, and (d) inslab events.**
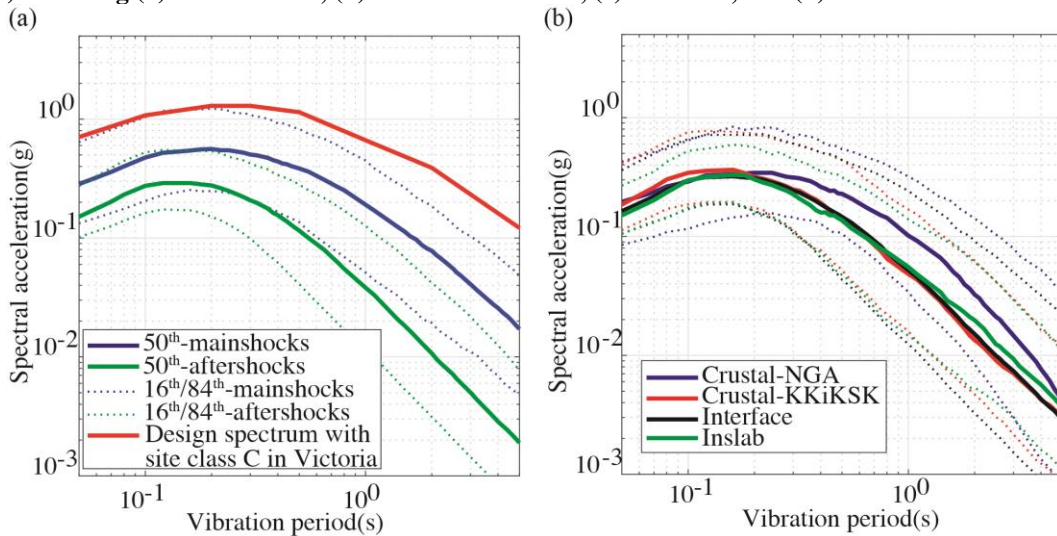
150
151   **Figure 3. Response spectra (a) of mainshocks and aftershocks with 16th, 50th, and 84th percentiles, and design**
152   **spectrum with site class C in Victoria (b) of different earthquake types from both mainshocks and aftershocks**
153   **with 16th, 50th, and 84th percentiles.**

4

2.3   UBC-SAWS model

The UBC-SAWS model is a structural model of typical wood-frame houses in British Columbia, Canada [30]. It is based on the SAWS model [31,32] with modifications of the model parameters for Canadian wooden house construction. The basic assumptions of the UBC-SAWS model are: (1) floor and roof diaphragms are rigid (length = 7.62 m, width = 6.10 m, and height = 2.74 m), (2) bi-directional horizontal seismic excitations are considered but ignoring vertical excitations, and (3) shear walls are represented by nonlinear springs, hysteresis of which is characterised by the Cyclic Analysis SHEar Walls (CASHEW) model [33] (see **Figure 4**). The CASHEW model incorporates stiffness and strength degradation. However, no in-cycle degradation is considered in the hysteresis model. The parameters of the UBC-SAWS model were calibrated based on static and dynamic tests of wall panels with different configurations and shake-table tests of full-scale houses that were conducted at the University of British Columbia [30]. The sheathing materials of the shear wall include horizontal board (shiplap), gypsum wallboard (GWB), plywood, oriented strand board (OSB), and stucco.

Based on different shear-wall configurations, four types of two-storey wood-frame houses are defined in the UBC-SAWS model: (1) House 1 with stucco/engineered OSB/GWB, (2) House 2 with engineered OSB/GWB, (3) House 3 with non-engineered OSB/GWB, and (4) House 4 with horizontal boards/GWB. The term 'engineered' for Houses 1 and 2 indicates that hold-downs and blocking of the wall panel are used to increase its seismic resistance and to meet the seismic code requirements. Due to the design layout of the house model in **Figure 4**(b) (e.g., dimensions of the house along x-axis and y-axis and locations of windows and doors), the stiffness along x-axis is smaller than that along y-axis, and the expected failure mode of the house models is the soft-storey collapse of the ground floor level due to larger openings. The fundamental vibration periods along x-axis of Houses 1-4 are 0.25 s, 0.3 s, 0.35 s, and 0.4 s, respectively, whereas those along y-axis are about 0.22 s for all houses [30]. In **Figure 4**(b), 16 walls (W1-W16), which are represented by nonlinear springs, are present along x-axis and y-axis on the ground and first floors. Shear-walls along x-axis are different for Houses 1-4 (W1 to W7), whereas shear-wall elements along y-axis are the same for the four house models (W8 to W16) [27]. The pushover analysis results of Houses 1-4 by using the inverse triangle load distribution are shown in **Figure 4**(c). The base shear ratio in vertical axis is the ratio of the base shear force and the total weight of the house. In terms of pushover curves, House 1 has the highest seismic capacity; Houses 2 and 3 have similar seismic resistance; and House 4 has the lowest seismic capacity. A recent study by [34] indicated that House 4 with horizontal boards is not suitable in high seismic regions and median collapse capacities of House 4 is reduced by 61% under long-duration motions in comparison with short-duration motions.
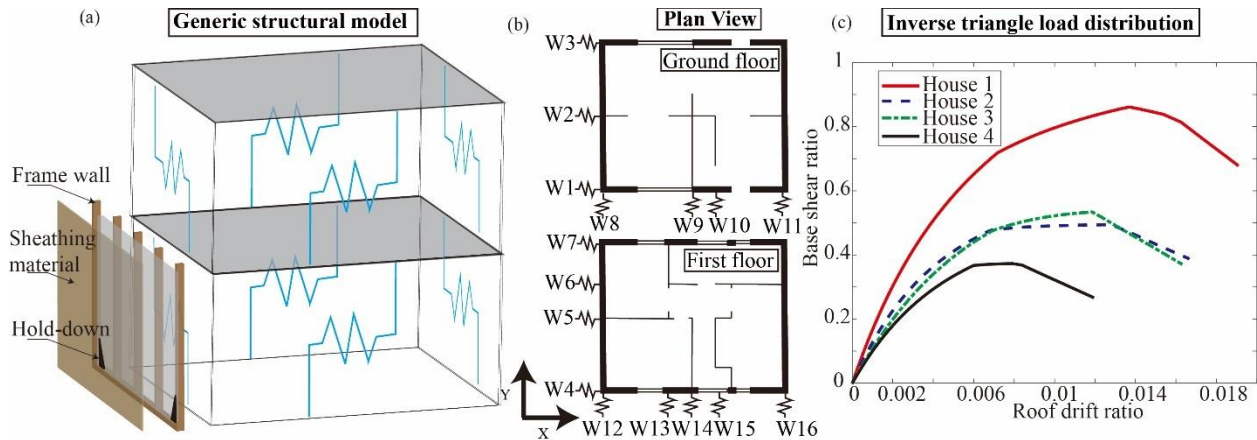
Figure 4. Illustration of the UBC-SAWS model: (a) generic model of wood-frame houses, (b) ground and first floor plans of wood-frame houses, and (c) pushover analysis of Houses 1-4.

2.4   Evaluation of *IM*s

To evaluate different *IM*s, various studies have focused on the efficiency, sufficiency, and relative sufficiency of *IM* [15,16,35]. Efficiency means that the prediction variability of *EDP* is small given *IM*, which can potentially reduce the number of structural response analyses. Consider a linear relationship between *IM* and *EDP* in logarithmic scale (base 10):

$$\log_{10}(EDP) = \log_{10}(a_{IM}) + b_{IM} \times \log_{10}(IM) \tag{1}$$

where a_{IM} and b_{IM} are the coefficients of the linear regression. The efficiency is calculated by [35]:

5

$$\beta_{IM} = \sqrt{\frac{\sum_{i=1}^{m}(\log_{10}(EDP_i) - \log_{10}(a_{IM} \times IM_i^{b_{IM}}))^2}{m-2}} \qquad (2)$$

Sufficiency of *IM* indicates that the *EDP* is independent of other explanatory variables, such as rupture distance and magnitude, when *IM* is taken into account. Therefore, if *IM* is sufficient, the inclusion of other variables, in addition to the main *IM*, does not affect the distribution of *EDP*. To evaluate the sufficiency of *IM*, the residual (*Res*$_{IM}$) between *IM* and *EDP* from **Equation (1)** is calculated as:

$$Res_{IM} = \log_{10}(EDP) - \log_{10}(a_{IM} \times IM^{b_{IM}}) \qquad (3)$$

Following that, the dependency of *Res*$_{IM}$ on rupture distance (R_{rup}) and magnitude (M_w) can be examined by:

$$Res_{IM} = c_{IM} + d_{IM} \times \log_{10}(R_{rup}) \qquad (4)$$
$$Res_{IM} = c_{IM} + d_{IM} \times M_w \qquad (5)$$

where c_{IM} and d_{IM} are the coefficients of the regression. The sufficiency of *IM* can be quantified by the significance level (p_{IM}-value) for d_{IM} [16].

Moreover, Jalayer *et al.* (2012) proposed relative sufficiency as a measure to compare the sufficiency between different IMs based on the concept of relative entropy from information theory. The relative sufficiency between two *IM*s is calculated by:

$$I(IM_j | IM_k) = \frac{1}{m} \times \sum_{i=1}^{m} \log_2 \left(\frac{\beta_{IM_k} \times \phi \left(\frac{\log_{10}(EDP_i) - \log_{10}(a_{IM_{j.i}} \times IM_{j.i}^{b_{IM_{j.i}}})}{\beta_{IM_j}} \right)}{\beta_{IM_j} \times \phi \left(\frac{\log_{10}(EDP_i) - \log_{10}(a_{IM_{k.i}} \times IM_{k.i}^{b_{IM_{j.i}}})}{\beta_{IM_k}} \right)} \right) \qquad (6)$$

where IM_j and IM_k represent different *IM*s, and β_{IM} is calculated from **Equation (2)**.

2.5 Seismic fragility functions

Using the selected ground motion records (Section 2.2) and the structural models (Section 2.3), 23,840 nonlinear dynamic analyses (= 4 house models × 596 MSAS sequences × 2 horizontal components × 5 scaling factors) are performed. The calculated structural responses are obtained for developing state-dependent seismic fragility functions as described in Section 2.1. The *pre-EDP*, *IM*, and *post-EDP* are selected and evaluated based on the different types of structural models and the preference of the modeller. The choice of the *IMs* and *EDPs* of SAWS model are further investigated in Section 3. To develop the post-DS fragility models in terms of associated *IM* and pre-DS, two methods are used as in Sections 2.5.1 and 2.5.2.

2.5.1 *Lognormal distribution*

The lognormal distribution has been widely used to fit seismic fragility curves [20]. The advantages of using the lognormal distribution for the fragility curve fitting are that (1) it is easy to apply because it has a simple format with a median and a logarithmic standard deviation as model parameters, and (2) it usually fits the data reasonable well [36]. The lognormal distribution is defined as:

$$P(DS_i) = \Phi \left(\frac{\ln \left(IM / \theta_{IM} \right)}{\beta_{IM}} \right) \qquad (7)$$

where Φ is the standard normal distribution, and θ_{IM} and β_{IM} are the median value and the standard deviation of the post-DS$_i$ fragility curves, respectively.

2.5.2 *Multinomial distribution*

The multinomial distribution has been applied in recent studies on fragility modelling [21,37]. In comparison with the lognormal distribution, the advantages of the multinomial distribution are that (1) it does not require binning of *IM*, so the pair of IM_i and post-DS$_i$ given the same pre-DS can be used directly to estimate the coefficients of the

244   multinomial distribution, and (2) since it can accommodate the hierarchical nature of damage state severity, derived
245   fragility curves do not intersect. The multinomial probability distribution is given by:

246

247    $P(DS_i) = \frac{1}{\prod_{j=1}^{nDS} y_{ij}!} \cdot \prod_{j=1}^{nDS} \pi_{ij}^{y_{ij}}$ (8)

248

249   where nDS is the total number of DS, y_{ij} is the number of data points in the ith IM falling in DS_j, and π_{ij} is the
250   probability that the ith observation is in DS_j. The systematic component of the model is represented by a link function:

251

252    $f(\pi_{ij}) = \theta_{j,0} + \sum_{k=i}^{nP} \theta_{j,k} \cdot \chi_k$ (9)

253

254   where θ is the regression parameter, nP is the number of explanatory variables χ. The explanatory variable can be IM,
255   structure type, and pre-DS if a large number of data points are available. Taking the mainshock fragility curves with
256    $DS_{0:n}$ as an example, $\theta_{j,0}$ is the intercept terms for the relative probability of DS_i given the reference $DS_{i+1:n}$. $\theta_{j,k}$ is the
257   coefficient of the explanatory variable, which is the mainshock IM in this example, and shows the probability of DS_i
258   versus $DS_{i+1:n}$ in the log scale as the IM increases.

259

260   ## 3 EVALUATION OF *EDP – IM* TRIPLETS USING REAL GROUND MOTION RECORDS

261   This section presents the preliminary exploratory phases of the model development by introducing *pre-EDP*,
262   investigating the suitability of *EDPs* for *pre-EDP* and *post-EDP*, and evaluating the efficiency and sufficiency of *IMs*.

263

264   ### 3.1   Pre-EDP
265   The conventional seismic fragility assessment for mainshock ground motions requires IM and *post-EDP* (e.g., only
266   event$_1$ in **Figure 5**(a)). To derive state-dependent aftershock fragility curves, a suitable *pre-EDP* needs to be specified.
267   **Figure 5**(a) illustrates a MSAS sequence from the Tohoku sequence, and **Figure 5**(b) and (c) display the structural
268   displacement response time-history and hysteretic response, respectively, using the UBC-SAWS model for W1 on the
269   ground floor of House 4.
270   Since the failure mode of the SAWS model is the soft-storey collapse of the ground floor level, three *EDPs*
271   suitable to describe such a mechanism are selected: (a) the maximum inter-storey drift (MaxISDR) at the first level,
272   (b) the residual inter-storey drift (ResISDR) at the first level, and (c) the maximum difference between MaxISDR and
273   ResISDR (MaxIISDR) at the first level. **Figure 5**(b) shows the maximum, residual, and maximum incremental
274   displacements of W1 for an illustrative earthquake sequence consisting of 3 events. MaxISDR$_1$ and MaxIISDR$_1$ of the
275   first event are identical, because the residual displacement before the first event is zero. If the residual displacement
276   is small, MaxIISDR becomes similar to MaxISDR.
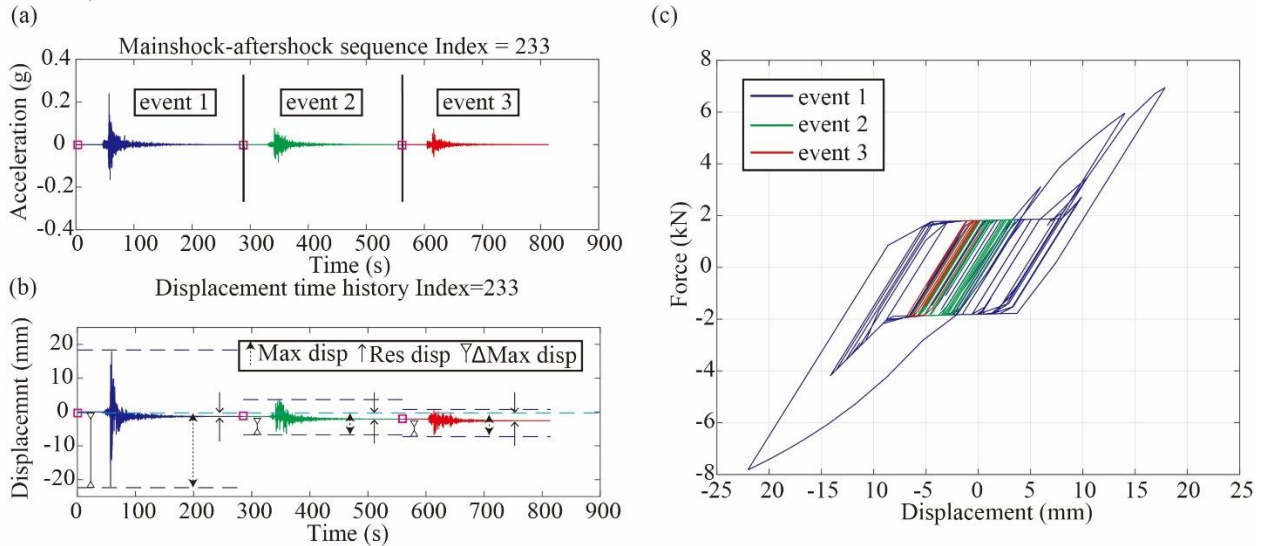
277
278   **Figure 5. (a) An example of the 2011 Tohoku mainshock-aftershock sequence with (b) the displacement
279   response time-history of House 4 of the maximum displacement (Max disp), the residual displacement (Res
280   disp) and the incremental maximum displacement (Δ Max disp), and (c) hysteretic response plot of Events 1-3.**

3.2   Evaluation of EDPs

Different combinations of *EDPs* for pre- and post-earthquake conditions are assessed by focusing upon three *EDPs*, i.e., MaxISDR, ResISDR, and MaxIISDR. In total, 9 combinations of *pre-EDP* and *post-EDP* are considered: Case 1-MaxISDR and post-MaxISDR, Case 2-pre-MaxIISDR and post-MaxISDR, Case 3-pre-ResISDR and post-MaxISDR, Case 4-pre-MaxISDR and post-MaxIISDR, Case 5-pre-MaxIISDR and post-MaxIISDR, Case 6-pre-ResISDR and post-MaxIISDR, Case 7-pre-MaxISDR and post-ResISDR, Case 8-pre-MaxIISDR and post-ResISDR, and Case 9-pre-ResISDR and post-ResISDR. These are displayed as a scatter plot where each *pre-EDP – post-EDP* point is associated with Sa(T=0.3 s) as *IM* (i.e. the coloured grading in **Figure 6**). According to **Figure 6**(a) and (b), the plots of *pre-EDP – IM – post-EDP* datasets from Cases 1 and 2 are similar. This is because (1) $MaxISDR_1$ and $MaxIISDR_1$ of the first event are identical given the residual displacement before the first event is zero, and (2) if the residual displacement is small, the MaxISDR and MaxIISDR tend to be similar. The same observation can be seen from Cases 4 and 5, and Cases 7 and 8.
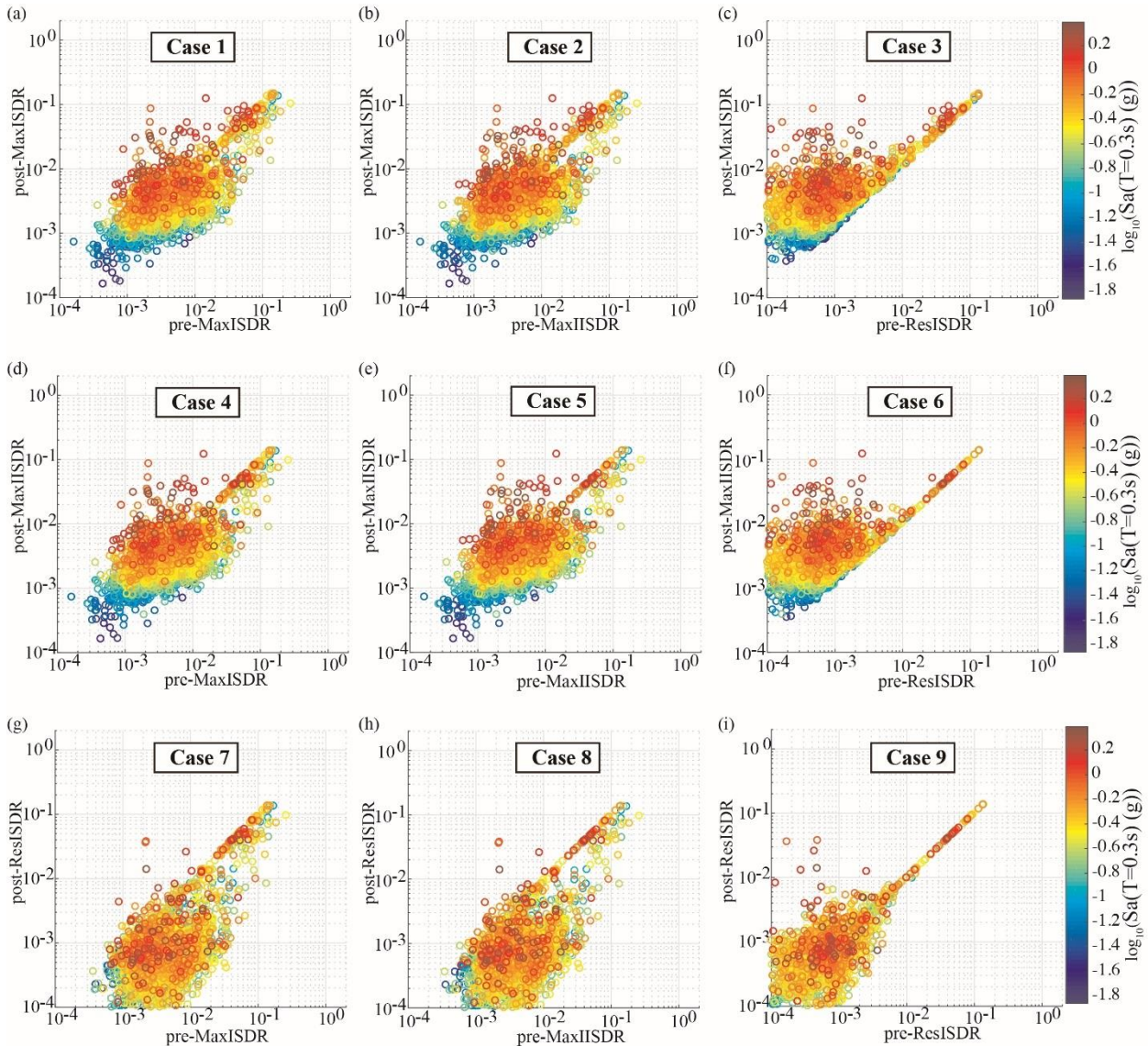
Figure 6. Plots of 9 cases of post-*EDP*s against pre-*EDP*s for House 4. (a) pre-MaxISDR and post-MaxISDR, (b) pre-MaxIISDR and post-MaxISDR, (c) pre-ResISDR and post-MaxISDR, (d) pre-MaxISDR and post-MaxIISDR, (e) pre-MaxIISDR and post- MaxIISDR, (f) pre-ResISDR and post-MaxIISDR, (g) pre-MaxISDR and post-ResISDR, (h) pre-MaxIISDR and post-ResISDR, and (i) pre-ResISDR and post-ResISDR.

8

300   Individual *pre-EDP*$_i$ should represent the DS of the structure from event$_1$ to event$_i$. In other words, since *IM*
301   is the only input of the current fragility simulation framework, *pre-EDP* that only represents the DS of individual
302   event$_i$ is not suitable for the state-dependent aftershock fragility curves. In this regard, MaxIISDR$_i$ that only describes
303   the relative DS between event$_{i-1}$ and event$_i$ may not be appropriate as *pre-EDP*. Based on that, Cases 2, 5, and 8 are
304   excluded from fragility fitting.
305   An ideal pair of *pre-EDP* and *post-EDP* should retain as many *IM–EDP* points as possible in fitting the
306   fragility curves robustly, and a higher *pre-EDP* should correspond to a higher *post-EDP* to represent the cumulative
307   damage due to an earthquake sequence. To include more *IM–EDP* points for the development of the fragility curves,
308   the *EDP* pairs of Cases 3, and 6 are more suitable than Cases 1, 4, 7, and 9. This is because the points in Cases 1, 4,
309   7, and 9 need to be divided into two parts which are *pre-EDP > post-EDP* and *pre-EDP < post-EDP*, respectively.
310   The former would be no damage scenario and only the latter part can be used for the aftershock fragility development.
311   On the other hand, when Cases 3 and 6 are considered in **Figure 6**(c) and (f), since the absolute maximum displacement
312   is always larger than the absolute residual displacement, all points can be used for the development of the fragility
313   curves, resulting in more robust curve fitting (i.e., all points are above the bisector of the quadrant).
314   Based on these considerations, Cases 3 and 6 are suitable options for the development of aftershock fragility
315   curves. However, an issue of adopting Case 6 is that the post-DS definitions of MaxIISDR may need to be changed
316   with pre-ResISDR. In other words, the DS associated with MaxIISDR is not constant given different pre-DSs, because
317   MaxIISDR$_i$ only represents the response of event$_i$. Considering MaxIISDR has not been widely used for aftershock
318   risk assessment in comparison with MaxISDR, in the subsequent part of this study only Case 3 (pre-ResISDR and
319   post-MaxISDR) is considered to represent *pre-EDP* and *post-EDP*.
320
321   **3.3   Evaluation of *IM*s**
322   To evaluate different *IMs*, metrics for efficiency, sufficiency, and relative sufficiency are calculated for Sa(T=0.05-5
323   s), AI, CAV, PGV, and SI [16,35,38]. The non-collapse *EDP* values [39] of House 4 are used for the evaluation of
324   *IMs* from the unscaled records of MSAS sequences, because the majority of the wood-frame houses in British
325   Columbia are classified as House 4 with non-seismic resistance [22,30].
326   The efficiency is examined based on [35]. A small standard deviation (β$_{IM}$) in **Equation (7)** indicates less
327   variability of the *IM–EDP* relationship (i.e., higher predictability). The values of β$_{IM}$ in a range of 0.2 to 0.3 and 0.3
328   to 0.4 are considered as a good and acceptable *IM* in terms of efficiency, respectively [40]. According to **Figure 7**(a),
329   Sa(T=0.3-0.5 s), PGV, and SI are more efficient than others for House 4.
330   Next, the sufficiency (p$_{IM}$) of *IMs* is checked against source parameters (rupture distance and magnitude) for
331   House 4. p$_{IM}$ captures the statistical independence between the source parameters and *IM* given p$_{IM}$>0.05. The
332   sufficiency of *IMs* in terms of rupture distance and magnitude is shown in **Figure 7**(b) and (c), respectively. Sa with
333   periods 0.2 to 2 s, PGV, and SI are good candidates of *IM*. On the other hand, Sa with periods 0.05-0.2 s and 2-5 s,
334   AI, and CAV show a high dependence on the source parameters, which indicates that these *IMs* are not appropriate
335   for use as sole *IM* for the fragility curve fitting of the wood-frame houses.
336   The relative sufficiency (I) is plotted in **Figure 7**(d) to rank different *IMs* for House 4. The fundamental
337   period of the wood-frame house (T=0.3 s) is considered as a reference *IM*, therefore, the relative sufficiency of
338   Sa(T=0.3 s) is 0. Sa values with periods T=0.32-1 s, PGV and SI have superior performance than Sa(T=0.3 s).
339   Especially, Sa(T=0.4-0.5 s) and PGV have the highest relative entropy. This suggests the period elongation of the
340   damaged structure in comparison with the fundamental period of 0.3 s. Since the most suitable *IMs* are in the range of
341   0.3-0.5 s and PGV shows a good performance of House 4, in this study Sa (T=0.3 s and 0.5 s) and PGV are used to
342   derive the state-dependent fragility curves in Section 4. In addition, the selection of *IM* should also be related to the
343   availability of the ground motion prediction equation (GMPE), when the developed fragility models are implemented
344   for seismic risk assessments. Although PGV is not widely used for the subduction GMPEs based on the global dataset
345   [41], other GMPEs for the CSZ have considered PGV as the output [42]. SI is also an appropriate *IM* based on the
346   results of sufficiency and efficiency. However, SI is calculated by taking the integral of spectral accelerations over a
347   period range from 0.1 to 2.5 s, which requires a high computational cost with the spatial correlation. In addition, the
348   correlations between periods are also necessary, therefore, in this study SI is not considered in the development of
349   aftershock fragility curves.
350
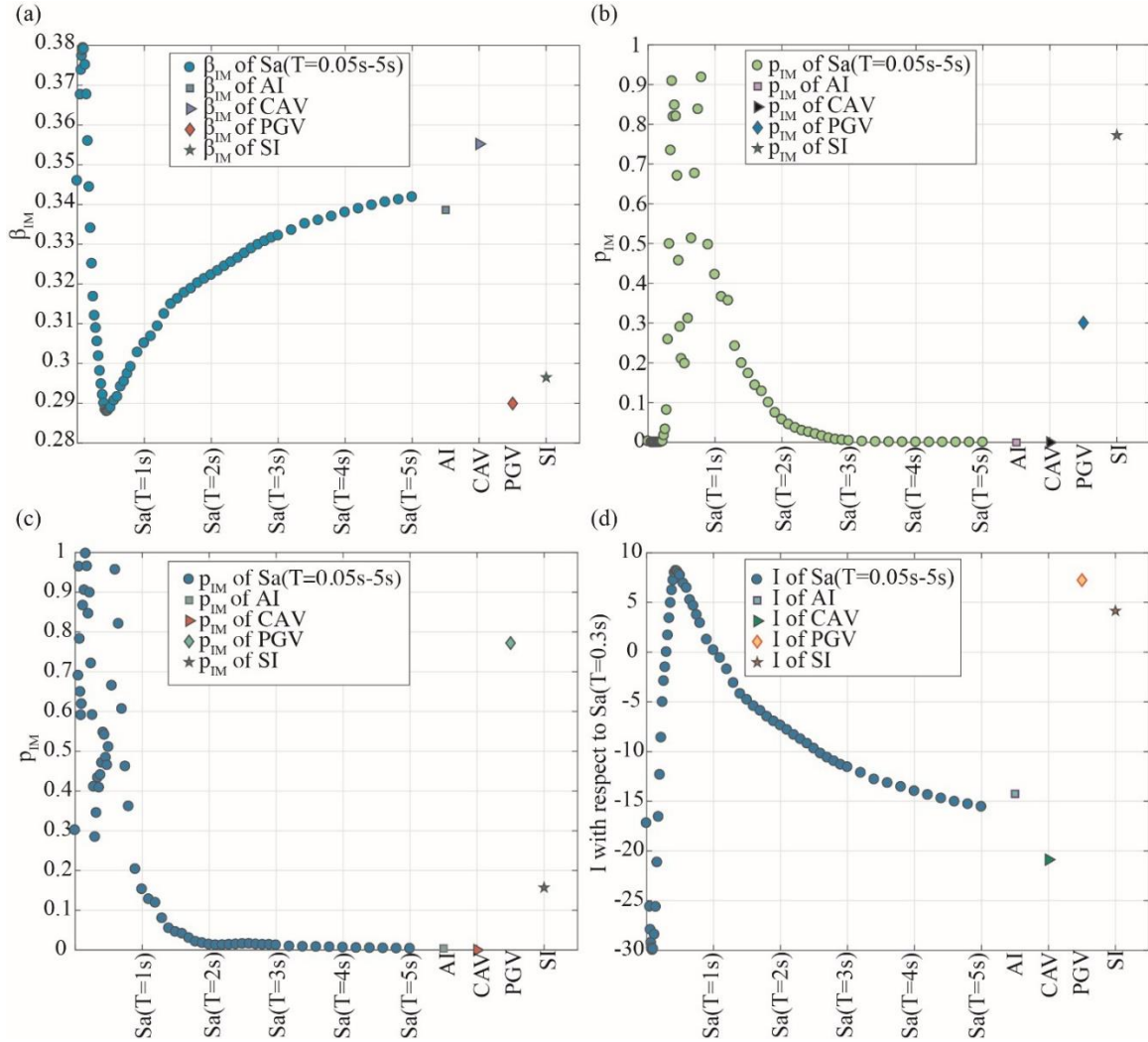
Figure 7. Plot of (a) efficiency (β_{IM}), sufficiency (p_{IM}) for (b) rupture distance and (c) magnitude, and (d) relative sufficiency (I) of each IM (Sa(T=0.05-5 s), AI, CAV, PGV, and SI) given the non-collapse EDP with unscaled records for House 4.

4 STATE-DEPENDENT FRAGILITY MODELLING

4.1 Definitions of pre-DS and post-DS

This subsection defines DSs in terms of pre-ResISDR and post-MaxISDR of Houses 1-4. Various studies investigated the relationship between ResISDR and MaxISDR for different types of structures, e.g., moment resisting steel frames and non-ductile reinforced concrete buildings [43,44]. For wood-frame houses, a FEMA study [45] defined performance level (PL) of wood stud walls based on MaxISDR. MaxISDR thresholds with PL_1-1%, PL_3-2%, and PL_5-3% are considered as immediate occupancy, life safety, and collapse prevention, respectively. In [46], the DSs of the wood-frame house associated with MaxISDR thresholds 1%, 2%, 4.5%, and 7% were defined as minor damage, significant damage, major damage, and collapse risk, respectively. In terms of the collapse state associated with MaxISDR, the collapse state of the SAWS model was defined as MaxISDR>7% in [39]. Considering different shear wall types of wood-frame houses and record durations, in [34] the collapse state of the wood-frame houses was defined based on the short and long durations of the records (same hysteretic model as this study but with modified hysteretic parameters). Regarding the DSs associated with ResISDR, $PL_{1,3,5}$ of wood stud walls were considered with the ResISDR thresholds with 0.25%, 1%, and 3% [45], while ResISDR of 0.2%, 0.5%, 1%, and 2% were suggested for $DS_{1-4FEMA}$ in [47]. In terms of building tagging for the post-earthquake evaluation, three tagging levels are usually considered, which are Green tag (unrestricted access), Yellow tag (restricted access), and Red tag (no access) [4].

373   Given the pushover analysis results of Houses 1-4 are significantly different in **Figure 4**(c), the DS thresholds
374 of each house model should be defined individually based on the literature and the *IM–EDP* results from this study.
375 The following procedures are carried out to define the DSs with MaxISDR and ResISDR of Houses 1-4 by first
376 determining the collapse states of ResISDR and MaxISDR:

377   •   The collapse state associated with MaxISDR for Houses 1-4 is defined by taking the average collapse state
378   limits of short and long record durations from [34], which is 7%, 6%, 6%, and 5.5% for Houses 1-4 (**Table**
379   **1**). This is because the ground motion records used in that study include both short- and long-duration records
380   and the application of the fragility curves would focus on both crustal and subduction-zone earthquakes.

381   •   The collapse state associated with ResISDR for Houses 1-4 is determined by the *IM–EDP* results from this
382   study. The 3D dataset including pre-ResISDR, Sa(T=0.3 s), and post-MaxISDR is binned according to pre-
383   ResISDR expressed in terms of percentage (i.e., [0; 0.3], [0.3; 0.5], [0.5; 1], [1; 2], [2; 3], [3; 4], [4; 5], [5;
384   6], [6; 7], and [7; 8]). The linear regression of log(non-collapsed post-MaxISDR) and
385         $a_{dsRes}+b_{dsRes}\log(Sa(T=0.3 \text{ s}))$ given each binned pre-ResISDR is obtained, where a_{dsRes} and b_{dsRes} are the
386   regression coefficients. The slope (b_{dsRes}) of linear regression is used to detect the change of pre-ResISDR.
387   Since the higher Sa(T=0.3 s) results in higher MaxISDR and ResISDR, the collapse state associated with
388   ResISDR is determined when the slope (b_{dsRes}) of MaxISDR against Sa(T=0.3 s) given the binned pre-
389   ResISDR is less than 0.1, which leads to 4%, 4%, 3%, and 3% for Houses 1-4.

391 **Table 1. Collapse state limits of Houses 1-4.**

	House 1	House 2	House 3	House 4
ResISDR	4%	4%	3%	3%
MaxISDR	7%	6%	6%	5.5%

393   By having the collapse state limits of ResISDR and MaxISDR, the ratios between three tagging levels and
394 collapse state are provided in **Table 2** based on the DS descriptions [4,45–47]. Green tag (DS$_1$) can be regarded to be
395 equivalent as immediate occupancy [4]. Yellow tag (DS$_2$) is the intermediate DS between life safety and collapse
396 prevention, because Yellow tag is defined for only acceptable entry for workers doing maintenance which is beyond
397 the life safety [3]. Red tag (DS$_3$) is the intermediate DS between collapse prevention and collapse because Red tag
398 forbids assess to a damaged building and the building is assumed to be near collapse. The description of each DS is
399 also summarised in **Table 2** based on [45], the Static and Dynamic Testing of Shear Wall Panels Project for the UBC-
400 SAWS model [48], and the Earthquake 99 Wood-frame House Project EQ 99 Project [30]. Wall components that are
401 described in **Table 2**, including wall frame, sheathing material, and hold-down, are shown in **Figure 4**(a).

403 **Table 2. Summary of damage states associated with the lower limits of ResISDR and MaxISDR (CS=collapse**
404 **state).**

	No damage (DS$_0$)	Green tag (DS$_1$)		Yellow tag (DS$_2$)		Red tag (DS$_3$)
ResISDR	0.01%	0.10×CS		0.30×CS		0.70×CS
MaxISDR	0.01%	0.10×CS		0.30×CS		0.70×CS
Performance level	No damage	Immediate occupancy	Life safety		Collapse prevention	Collapse
Description of damage state	No damage is observed.	Minor cracks are observed in sheathing materials. Hairline cracks are observed in external walls.	Studs are attached to the sheathing at end but are easy to bend in the middle. Nails partially loose and are attached to the stud for OSB of Houses 1-3. Sheathing is detached in the middle. Glass is partially damaged.		Studs are not attached to sheathing for some shear walls. Nails are pulled out on the sheathing. Some sheathing failure. Some fasteners on GWB are pushed. Glass is significantly damaged. Hold downs are loose for Houses 1-2.	Ground floor of the house is collapsed.

406   A scatter plot of the evaluated *EDPs* (post-MaxISDR versus pre-ResISDR) with the unscaled records for
407 House 4, which is colour-coded based on Sa(T=0.3 s), is shown in **Figure 8**. Although all 596 MSAS sequences are

11

408 included in the structural analysis, small sample sizes with the number of points less than 100 are observed with pre-
409 DS$_{1-2}$. This indicates that the scaling of records is necessary.
410
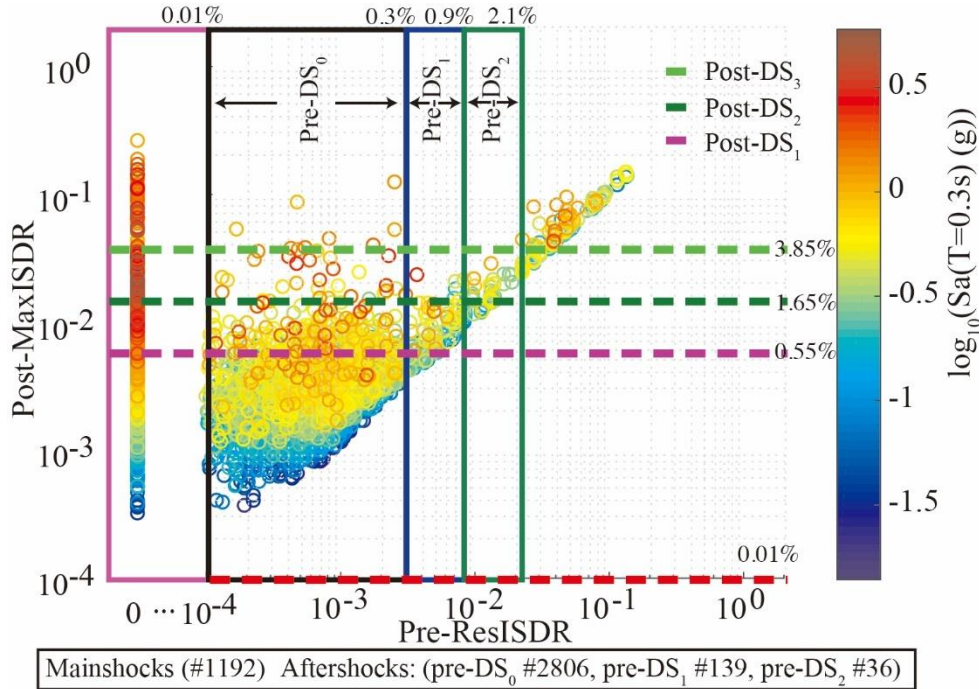
411
412 **Figure 8. Plot of post-MaxISDR against pre-ResISDR with Sa(T=0.3 s) for House 4 using unscaled records. The**
413 **number of points from mainshock is 1,192, and the number of points from aftershocks given pre-DS$_0$, pre-DS$_1$,**
414 **and pre-DS$_2$ is 2,806, 139, and 36, respectively.**
415

416 **4.2   Procedures to develop aftershock fragility curves of wood-frame houses**
417 Due to the insufficient data points of pre-DS$_{1-2}$ in **Figure 8**, the *pre-EDP*, *IM*, and *post-EDP* of each event during the
418 mainshock-aftershock sequence with the scaling factors 1 to 5 are used; this leads to 4,562×5=22,810 points in total,
419 including 5,960 and 16,850 data points for mainshocks and aftershocks, respectively. Since the frequency content of
420 mainshocks is significantly different from that of the aftershocks (**Figure 3**), the mainshock fragility curves and the
421 state-dependent aftershock fragility curves are produced separately. A plot of post-MaxISDR against Sa(T=0.3 s) for
422 mainshocks only with the scaling factors 1 to 5 given pre-ResISDR=0% with post-DS$_{1-3}$ is shown in **Figure 9**(a).
423   The new approach to develop the state-dependent fragility curves of aftershocks is as follows:
424   1.   The 16,850 data points in **Figure 9**(b) are classified into pre-DS$_{0-2}$ based on the pre-ResISDR bins defined
425   in **Table 2**. The subplots of MaxISDR against Sa(T=0.3 s) for pre-DS$_{0-2}$ are shown in **Figure 10**(a)-(c).
426   2.   For each pre-DS$_i$ (i=0, 1, and 2), the number of post-MaxISDR > post-DS$_i$ (i=1, 2, and 3) (i.e., exceeding the
427   damage threshold in terms of MaxISDR in **Table 2**) is counted.
428   3.   Two fragility functions are used to develop the fragility curves:
429   a.   For the lognormal distribution, fixed *IM* bins are defined for all pre-DSs in **Figure 10** to fit
430   consistently for all pre-DS$_i$ given the same post-DS$_i$. The fraction of *post-EDP* > post-DS$_i$ (i=1, 2,
431   and 3) from the lognormal distribution (e.g., [20]) is used to develop the fragility curves associated
432   with *IM* for each pre-DS using the maximum likelihood estimation (MLE).
433   b.   The multinomial fitting based on the MLE is used to develop the post-DS curves with *IM* given the
434   same pre-DS [21,37,49].

12
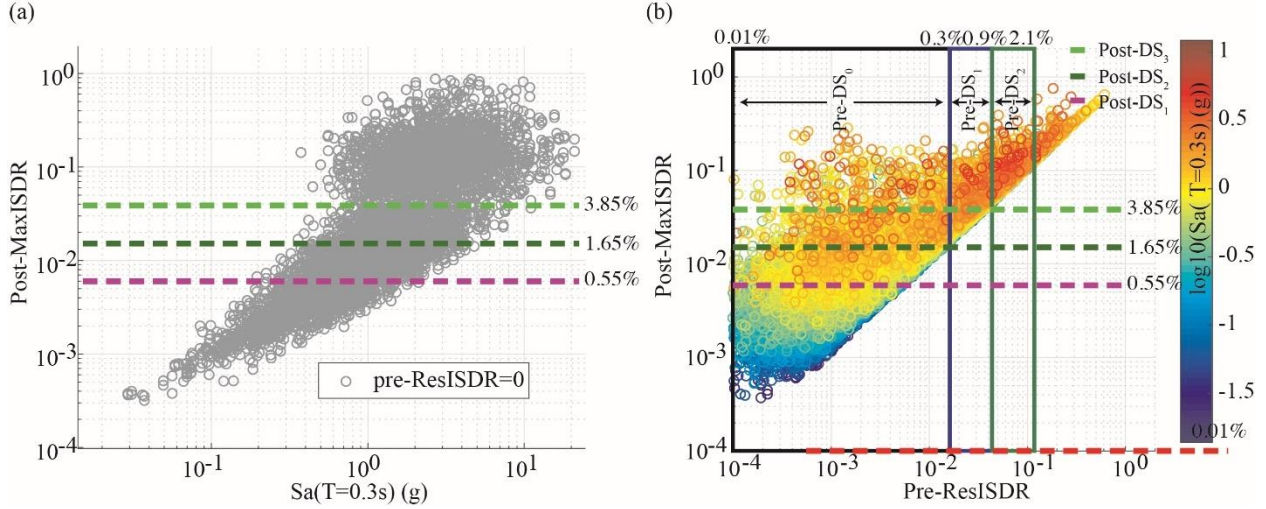
Figure 9. (a) Plot of post-MaxISDR against Sa(T=0.3 s) of House 4 for mainshocks only (596 records × 2 horizontal components × 5 scaling factors=5,960 points). (b) Plot of post-MaxISDR against pre-ResISDR for aftershocks (1,685 records × 2 horizontal components × 5 scaling factors=16,850 points).
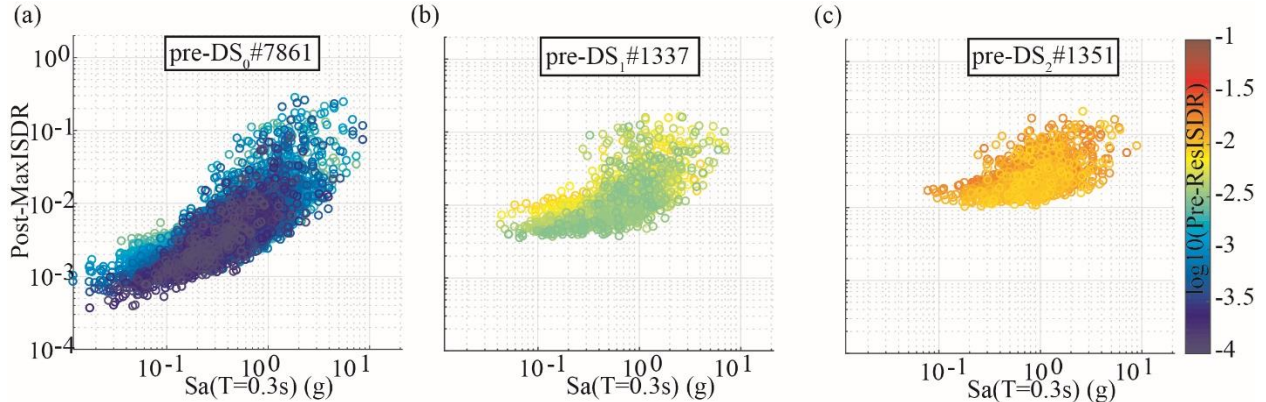

Figure 10. Plot of post-MaxISDRs against IM(T=0.3 s) for House 4 with scaling factors 1 to 5 given pre-ResISDR (a) 0.01%-0.3% (7,861 points), (b) 0.3%-0.9% (1,337 points), and (c) 0.9%-2.1% (1,351 points).

4.3   Comparison of aftershock fragility curves with Sa(T=0.3 s), Sa(T=0.5 s), and PGV

Since the state-dependent fragility curves are developed based on post-DSs given the same pre-DS, post-DSs from the same pre-DS should not intersect. Therefore, only the same post-DS$_i$ given pre-DS$_0$ to pre-DS$_{i-1}$ are presented in the following fragility curve plots. To make a fair comparison, the state-dependent fragility curves of post-DS$_3$ given pre-DS$_0$ to pre-DS$_2$ of House 4 with Sa(T=0.3 s), Sa(T=0.5 s), and PGV using the lognormal distribution are shown in **Figure 11**. The estimated median values (θ_{IM}) and standard deviations (β_{IM}) for post-DS$_{1-3}$ given pre-DS$_{0-2}$ with Sa(T=0.3 s), Sa(T=0.5 s), and PGV are summarised in **Table 3**. The state-dependent fragility curves with different fragility functions are presented in the next subsection (Section 4.4). The limit of x-axis is constrained by the maximum *IM* from the observed records.

The median values of Sa(T=0.3 s), Sa(T=0.5 s), and PGV decrease from pre-DS$_0$ to pre-DS$_2$ in **Table 3**, showing that the damaged house requires a low *IM* to reach the same post-DS. Although Sa(T=0.3 s) has been widely used as *IM* for the mainshock fragility curves [27], aftershock fragility curves with Sa(T=0.3 s) in **Figure 11**(a) are not well fitted by the lognormal distribution with the standard deviation larger than 1 for the Red tag (DS$_3$) in **Table 3**. On the other hand, in **Figure 11**(b) and (c), PGV and Sa(T=0.5 s) show better performances of aftershock fragility curves for representing the cumulative damage effects than Sa(T=0.3 s). PGV and Sa(T=0.5 s) cover higher exceeding probabilities of post-DS$_3$ from pre-DS$_{0-1}$ than Sa(T=0.3 s) in **Figure 11**(b) and (c), respectively. All logarithmic standard deviations for different *IMs* in **Table 3** are increased from pre-DS$_0$ to pre-DS$_2$, and the standard deviations of aftershock fragility curves of Sa(T=0.3 s) and Sa(T=0.5 s) are higher than 0.8. This might suggest that stronger records of aftershocks are needed to include more points in the fragility curve development for Sa(T=0.3 s) and

13

Sa(T=0.5 s) in the range from 2 g to 3 g. Large standard deviations (e.g., 0.79) of state-dependent fragility curves were also observed from the back-to-back approach with IDA [50]. On the other hand, PGV shows a better performance for the development of aftershock fragility curves with standard deviations lower than 0.6. Overall, PGV is the most suitable IM for the cumulative damage aftershock fragility curves of the wood-frame houses.
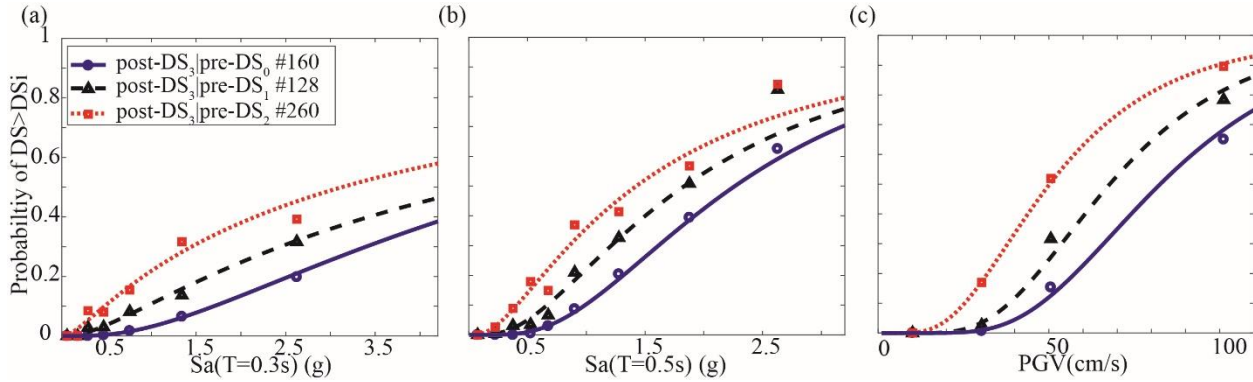
Figure 11. Plots of aftershock fragility curves for the post-DS$_3$ given pre-DS$_{0-2}$ with (a) Sa(T=0.3 s), (b) Sa(T=0.5 s), and (c) PGV based on pre-ResISDR and post-MaxISDR for House 4 and the lognormal distribution. The number of points exceeding post-DS$_3$ given pre-DS$_0$, pre-DS$_1$, and pre-DS$_2$ for House 4 is 160, 280, and 260, respectively.

Table 3. Median values (θ_{IM}) of mainshock-aftershock fragility curves for House 4 (standard deviations (β_{IM}) are shown in the parentheses) from the lognormal distribution.

	post-DS$_1$	post-DS$_2$	post-DS$_3$
House 4 (Sa(T=0.3 s))			
pre-DS$_0$ (MS)	0.51 (0.51)	1.24 (0.57)	1.83 (0.70)
pre-DS$_0$ (AS)	0.66 (0.62)	2.37 (0.80)	5.49 (0.92)
pre-DS$_1$ (AS)		1.26 (0.94)	4.71 (1.25)
pre-DS$_2$ (AS)			3.13 (1.47)
House 4 (Sa(T=0.5 s))			
pre-DS$_0$ (MS)	0.35 (0.30)	0.92 (0.32)	1.32 (0.46)
pre-DS$_0$ (AS)	0.33 (0.44)	1.04 (0.49)	2.26 (0.65)
pre-DS$_1$ (AS)		0.65 (0.65)	1.83 (0.79)
pre-DS$_2$ (AS)			1.43 (0.97)
House 4 (PGV)			
pre-DS$_0$ (MS)	17.84 (0.36)	44.73 (0.32)	63.35 (0.29)
pre-DS$_0$ (AS)	16.67 (0.47)	46.29 (0.45)	82.55 (0.43)
pre-DS$_1$ (AS)		28.93 (0.58)	67.80 (0.44)
pre-DS$_2$ (AS)			38.96 (0.60)

4.4 Comparison of aftershock fragility curves using the lognormal and multinomial distributions

In this subsection, the fragility curves using the multinomial distribution of House 4 of post-DS$_3$ given pre-DS$_0$ to pre-DS$_2$ with Sa(T=0.3 s), Sa(T=0.5 s), and PGV are shown in **Figure 12**(a), (b), and (c), respectively. All estimated parameters of the multinomial distribution are summarised in **Table 4**. Similar performances can be observed from the fixed IM bin counts of the lognormal distribution and multinomial distribution. Considering the inputs of the multinomial distribution fitting are IMs and post-DSs rather than the IM bins with certain exceeding probabilities from the lognormal distribution, the empirical distributions are counted such that the same number of data points of each bin is available. The number of data points in each bin is 5% of the total points given the same pre-DS but is constrained in the range of 50-200 in **Figure 12**. Although both fragility functions show good performances, the multinomial fitting is a better option. This is because the fixed IM bin counts from the lognormal distribution require a careful assessment of the histogram count of IMs given pre-DSs, and less than 10 IM bin counts are included to avoid the intersection of the same post-DS$_i$ given pre-DSs. On the other hand, the multinomial distribution only requires IM and

14

489 post-DSs given each pre-DS$_i$ to fit the curves progressively. Based on these considerations, the multinomial
490 distribution is used to develop the aftershock fragility curves for the rest of the house models in the next subsection.
491
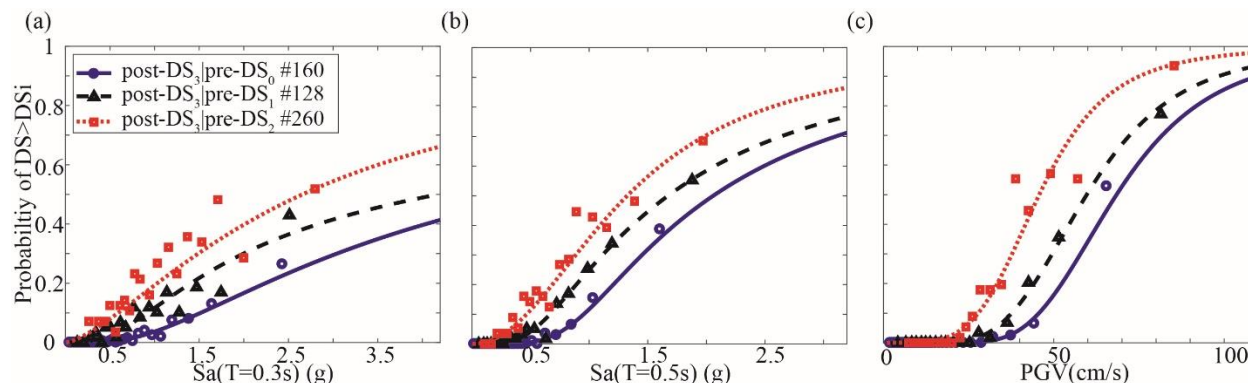
492
493 **Figure 12. Plots of aftershock fragility curves for the post-DS$_3$ given pre-DS$_{0-2}$ with (a) Sa(T=0.3 s), (b) Sa(T=0.5**
494 **s), and (c)PGV based on pre-ResISDR and post-MaxISDR for House 4 and the multinomial distribution. The**
495 **number of points exceeding post-DS$_3$ given pre-DS$_0$, pre-DS$_1$, and pre-DS$_2$ for House 4 is 160, 280, and 260,**
496 **respectively.**
497

498 **Table 4. Estimated parameters of mainshock-aftershock fragility curves of House 4 from the multinomial**
499 **distribution.**

	post-DS1	post-DS2	post-DS3
House 4 (Sa(T=0.3 s))			
pre-DS$_0$ (MS)	-2.48, -3.71	0.42, -2.75	-0.10, -1.34
pre-DS$_0$ (AS)	-1.42, -3.04	1.35, -1.87	1.25, -0.94
pre-DS$_1$ (AS)		0.31, -2.16	0.96, -0.76
pre-DS$_2$ (AS)			1.43, -1.46
House 4 (Sa(T=0.5 s))			
pre-DS$_0$ (MS)	-6.98, -6.75	-0.51, -5.66	0.15, -2.54
pre-DS$_0$ (AS)	-5.21, -4.70	-0.003, -3.58	1.18, -1.84
pre-DS$_1$ (AS)		-1.33, -2.93	0.77, -1.72
pre-DS$_2$ (AS)			0.59, -2.10
House 4 (PGV)			
pre-DS$_0$ (MS)	14.94, -5.18	21.76, -5.74	22.55, -5.54
pre-DS$_0$ (AS)	13.41, -4.82	18.15, -4.88	18.72, -4.47
pre-DS$_1$ (AS)		15.1806, -4.5396	17.63, -4.33
pre-DS$_2$ (AS)			16.91, -4.42

500
501 **4.5   Aftershock fragility curves of Houses 1-3 with PGV**
502 The plots of state-dependent fragility curves for Houses 1-3 are provided in **Figure 13**. By considering PGV as *IM*
503 with the multinomial distribution, the fragility curves of Houses 1-4 (**Figure 12**(c) and **Figure 13**) show a good
504 agreement with the description of seismic resistance in Section 2.3. For example, by looking at the PGV values with
505 50% exceeding probability of collapse state given intact conditions in **Figure 12**(c) and **Figure 13**, House 1 has the
506 highest PGV value (110 cm/s), whereas the median value of PGV for House 4 is 65 cm/s. This indicates the better
507 performance of the engineered OSB sheathing in comparison with horizontal board sheathing [34].
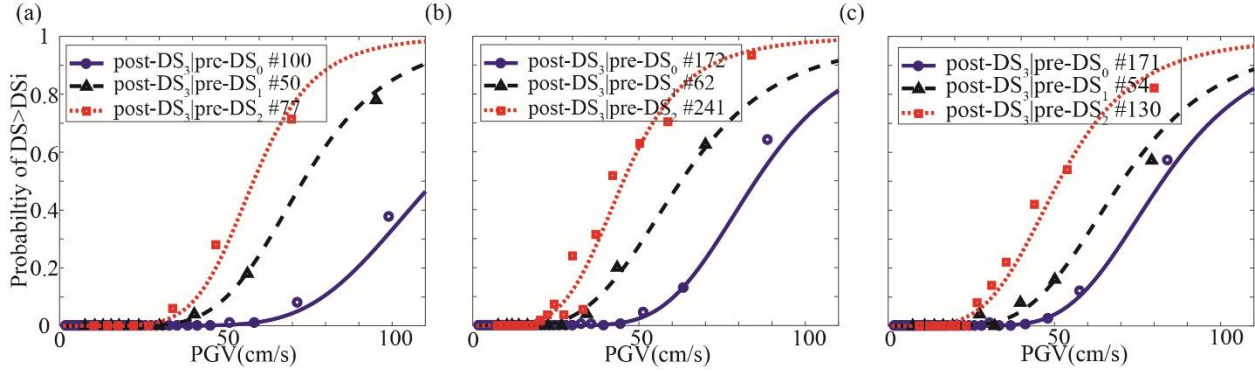508

509
510 **Figure 13. Plots of aftershock fragility curves for the post-DS$_3$ given pre-DS$_{0-2}$ with PGV based on pre-ResISDR**
511 **and post-MaxISDR for (a) House 1, (b) House 2, and (c) House 3 with the multinomial distribution.**

512
513 **Table 5. Parameters θ_1 and θ_2 from the multinomial distribution for Houses 1-3.**

	post-DS1	post-DS2	post-DS3
House 1 (PGV)			
pre-DS$_0$ (MS)	15.49, -4.29	25.40, -5.78	28.85, -6.17
pre-DS$_0$ (AS)	14.25, -4.28	17.70, -4.07	24.64, -5.30
pre-DS$_1$ (AS)		16.99, -4.80	23.57, -5.50
pre-DS$_2$ (AS)			26.06, -6.41
House 2 (PGV)			
pre-DS$_0$ (MS)	16.92, -5.16	24.23, -5.94	27.95, -6.33
pre-DS$_0$ (AS)	15.74, -5.10	19.94, -5.00	24.44, -5.54
pre-DS$_1$ (AS)		19.92, -6.18	17.46, -4.22
pre-DS$_2$ (AS)			18.30, -4.80
House 3 (PGV)			
pre-DS$_0$ (MS)	16.33, -5.15	23.48, -5.78	26.17, -5.98
pre-DS$_0$ (AS)	15.21, -5.08	19.14, -4.82	22.00, -5.04
pre-DS$_1$ (AS)		14.33, -4.04	19.19, -4.54
pre-DS$_2$ (AS)			17.44, -4.43

514
515 **4.6   Application for state-dependent fragility curves to the Cascadia subduction zone**
516 To demonstrate an application of the state-dependent fragility curves, an example of a M_w 9.0 mainshock followed by
517 a M_w 6.0 crustal aftershock [51] in the CSZ is considered. PGVs for the M_w 9.0 mainshock scenario (rupture distance
518 of 70 km) and the M_w 6.0 crustal aftershock scenario (Joyner and Boore distance of 8 km) are calculated for the City
519 of Victoria, Canada with V_{s30}=450 m/s using GMPEs [42,52].

520   Using the simulation-based seismic hazard and risk approach [53], the PGV from a M_w 9.0 event can be
521 applied to the MS fragility curves to estimate the post-DS$_{i,1}$ (post-DS$_i$ after the 1st event which is the same notation as
522 in **Figure 1**). The post-DS$_{i,1}$ due to the first event is equivalent as pre-DS$_{i,2}$ (pre-DS$_i$ before the second event).
523 Following that, pre-DS$_{i,2}$ and the PGV of the aftershock would be the input information to select the state-dependent
524 fragility curves of aftershocks to estimate the post-DS$_{i,2}$. Subsequently, more aftershocks can be considered to estimate
525 the DS of the house model after each subsequent aftershock. The state-dependent fragility curves allow to estimate
526 the DS of the house model after each event sustaining the same DS or reaching a higher level of DS given *IM*.

527   In total 10,000 simulations are carried out. Each simulation has PGVs of the M_w 9.0 mainshock followed by
528 the M_w 6.0 crustal aftershock. Following that, the PGV of mainshock and aftershocks are randomly sampled from the
529 fragility curves to calculate the DS after the mainshocks and aftershocks. The damage probabilities of Houses 1-4 by
530 the M_w 9.0 mainshock and the MSAS sequences based on 10,000 simulations are shown in **Figure 14**a and b,
531 respectively. By including the crustal aftershocks, the probabilities that Houses 1-4 are changed from DS$_0$ (no damage)
532 to DS$_1$ (Green tag) are 18.1%, 18.6%, 18.6%, and 14.0%. Compared with the damage probability of the mainshock,
533 additional 6.4%, 12.3%, 9.3%, and 12.3% of Houses 1-4 could change to DS$_2$ (Yellow tag) by the crustal aftershock,

16

534   whereas the probabilities that the crustal aftershock causes additional damage of DS_3 (Red tag) are 1.1%, 3.3%, 2.5%,
535   and 4.8% in comparison with the mainshock for Houses 1-4.
536
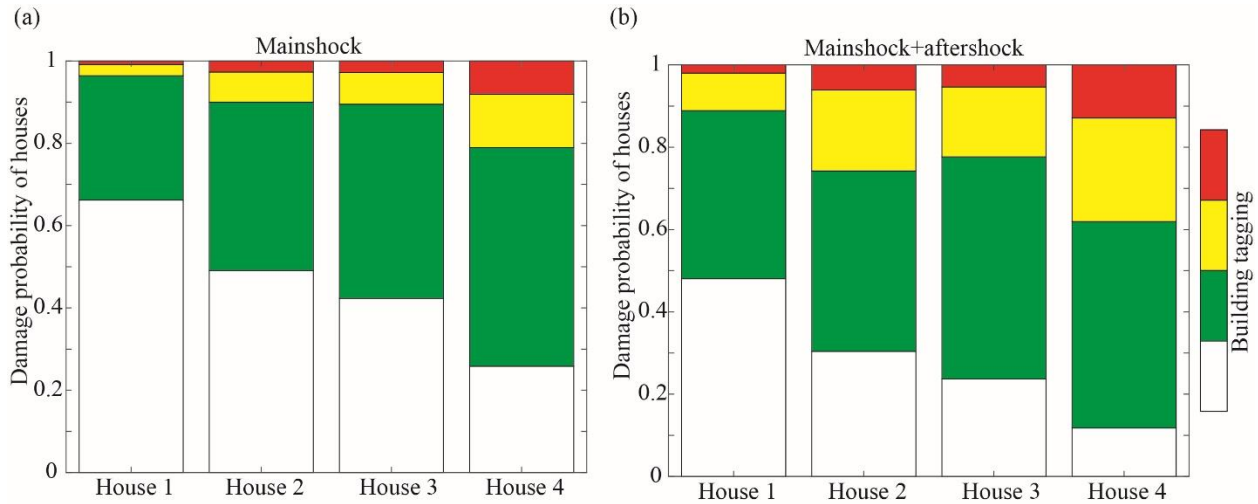
538   **Figure 14. Damage probability of Houses 1-4 by (a) M_w 9.0 mainshock with 70km rupture distance and (b) M_w**
539   **9.0 mainshock and M_w 6.0 crustal aftershock with Joyner-Boore distance=8 km and V_{s30}=450 m/s.**
540

5 CONCLUSIONS

543   This study developed a new approach to produce the state-dependent fragility curves. To capture the real
544 characteristics of aftershocks in the cumulative damage assessments of mainshock and aftershock sequences, the *pre-*
545 *EDP* combining with *IM* and *post-EDP* as a 3D dataset was introduced for developing the state-dependent aftershock
546 fragility curves. The UBC-SAWS model was used to demonstrate the new approach for the state-dependent fragility
547 curves of the wood-frame houses using 596 real MSAS records with cloud analysis. The selection of *IMs* (Sa, AI,
548 CAV, PGV, and SI) and *EDPs* (ResISDR, MaxISDR, and MaxIISDR) for wood-frame houses was discussed in this
549 study. To account for the cumulative damage after event$_n$, the pre-ResISDR and post-MaxISDR are considered to be
550 the most suitable *EDPs* to represent the *pre-EDP* and *post-EDP*, respectively. To evaluate different *IMs*, the efficiency,
551 sufficiency, and relative sufficiency were evaluated for each *IM*. Sa(T=0.3-0.5 s) and PGV show better performances
552 than other *IMs*.
553   The MSAS fragility curves were developed with pre-ResISDR and post-MaxISDR by considering *IMs*
554 (Sa(T=0.3 s), Sa(T=0.5 s), and PGV). PGV showed a better performance to capture the cumulative damage effects of
555 aftershocks for the wood-frame structure using real MSAS sequences than other *IMs*. Different fragility functions (the
556 lognormal and multinomial distributions) were also compared. The multinomial distribution was considered as more
557 suitable to fit the fragility curves than the lognormal distribution, because the former does not require careful bin
558 counts to avoid the intersections of aftershock fragility curves for post-DS conditioned on different pre-DSs.
559 Combining the building-tagging-based DS definitions with the multinomial distribution lead to the development of
560 robust aftershock fragility curves.
561   The limitations of the aftershock fragility curves include that (1) more destructive aftershock records should
562 be included to have a better fitting of fragility models with a smaller logarithmic standard deviation for Sa(T=0.3 s)
563 and Sa(T=0.5 s), (2) when more destructive aftershock records are included, ground motion records could be further
564 classified by earthquake types, so aftershock fragility curves can be developed by crustal and subduction-zone records
565 which represent the different spectra shapes between the crustal and subduction-zone earthquakes, and (3) the SAWS
566 model does not incorporate in-cycle degradation. A further investigation of the impact of in-cycle degradation on the
567 development of fragility curves is necessary in the future study.
568   The developed aftershock fragility curves of Houses 1-4 can be employed to estimate the DSs implementing
569 a spatiotemporal risk assessment for a M_w 9.0 mainshock triggering both crustal and subduction-zone aftershocks (e.g.,
570 [54]) in British Colombia, Canada. The evaluated PGV and real MSAS sequences facilitate the estimation of
571 cumulative damage of wood-frame houses. The outputs of the risk assessment provide not only the likelihood of the
572 DSs on the day of the inspection for building tagging [55] but also daily forecasts of the DSs in a short-time period
573 after the inspection day. This can be part of inspection combing with the conventional building tagging (e.g., residual

574 displacement check of the structure components) and providing additional information for the structural inspector. In
575 addition, a future direction of the development of state-dependent fragility curves could be to develop an approach to
576 construct 'realistic MS-AS sequences' either using real records with careful record selection or simulating records as
577 mainshock-aftershock sequence for the Cascadia subduction zone (e.g., [24]).
578
588
589 **REFERENCES**
590
591 1.   Goda K, Pomonis A, Chian SC, Offord M, Saito K, Sammonds P, *et al.* Ground motion characteristics and
592   shaking damage of the 11th March 2011 M w 9.0 Great East Japan earthquake. *Bulletin of Earthquake*
593   *Engineering* 2013; **11**(1): 141–170.
594 2.   Kazama M, Noda T. Damage statistics (Summary of the 2011 off the Pacific Coast of Tohoku Earthquake
595   damage). *Soils and Foundations* 2012; **52**(5): 780–792.
596 3.   Yeo GL, Cornell CA. Building tagging criteria based on aftershock PSHA. *13th World Conference on*
597   *Earthquake Engineering*, 2004.
598 4.   Bazzurro P, Cornell CA, Menun C, Motahari M. Guidelines for seismic assessment of damaged buildings.
599   *13th World Conference on Earthquake Engineering*, 2004.
600 5.   Yeo GL, Cornell CA. Post-quake decision analysis using dynamic programming. *Earthquake Engineering &*
601   *Structural Dynamics* 2009; **38**(1): 79–93.
602 6.   Iervolino I, Giorgio M, Chioccarelli E. Closed-form aftershock reliability of damage-cumulating elastic-
603   perfectly-plastic systems. *Earthquake Engineering & Structural Dynamics* 2014; **43**(4): 613–625.
604 7.   Ebrahimian H, Jalayer F, Asprone D, Lombardi AM, Marzocchi W, Prota A, *et al.* A performance-based
605   framework for adaptive seismic aftershock risk assessment. *Earthquake Engineering & Structural Dynamics*
606   2014; **43**(14): 2179–2197.
607 8.   Goldfinger C, Nelson CH, Morey a. E, Joel E J, Patton J, Karabanov E, *et al.* Turbidite event history —
608   methods and implications for holocene paleoseismicity of the Cascadia Subduction Zone. *US Geological*
609   *Survey Professional Paper 1661-F* 2012: 170 p.
610 9.   Verderame GM, Ricci P, De Luca F, Del Gaudio C, De Risi MT. Damage scenarios for RC buildings during
611   the 2012 Emilia (Italy) earthquake. *Soil Dynamics and Earthquake Engineering* 2014; **66**: 385–400.
612 10.   Luco N, Bazzurro P, Cornell CA. Dynamic versus static computation of the residual capacity of a
613   mainshock-damaged building to withstand an aftershock. *13th World Conference on Earthquake*
614   *Engineering* 2004.
615 11.   Jalayer F, Ebrahimian H. Seismic risk assessment considering cumulative damage due to aftershocks.
616   *Earthquake Engineering & Structural Dynamics* 2017; **46**(3): 369–389.
617 12.   Raghunandan M, Liel AB, Luco N. Aftershock collapse vulnerability assessment of reinforced concrete
618   frame structures. *Earthquake Engineering & Structural Dynamics* 2015; **44**(3): 419–439.
619 13.   Goda K. Record selection for aftershock incremental dynamic analysis. *Earthquake Engineering &*
620   *Structural Dynamics* 2015; **44**(7): 1157–1162.
621 14.   Cornell CA, Asce M, Jalayer F, Hamburger RO, Foutch D a. Probabilistic basis for 2000 SAC Federal
622   Emergency Management Agency steel moment frame guidelines 2002; **128**(4): 526–533.
623 15.   Luco N, Cornell CA. Structure-specific scalar intensity measures for near-source and ordinary earthquake
624   ground motions. *Earthquake Spectra* 2007; **23**(2): 357–392.
625 16.   Luco N. Probabilistic seismic demand analysis, SMRF connection fractures, and near-source effects, *Ph.D.*
626   *thesis*, Department of Civil and Environmental Engineering, Stanford University, 2002.
627 17.   Bradley BA. Empirical equations for the prediction of displacement spectrum intensity and its correlation
628   with other intensity measures. *Soil Dynamics and Earthquake Engineering* 2011; **31**(8): 1182–1191.
629 18.   Vamvatsikos D, Cornell CA. Incremental dynamic analysis. *Earthquake Engineering & Structural*

630   *Dynamics* 2002; **31**(3): 491–514.

631   19.   Goda K, Salami MR. Inelastic seismic demand estimation of wood-frame houses subjected to mainshock-
632   aftershock sequences. *Bulletin of Earthquake Engineering* 2014; **12**(2): 855–874.

633   20.   Baker JW. Efficient analytical fragility function fitting using dynamic structural analysis. *Earthquake*
634   *Spectra* 2015; **31**(1): 579–599.

635   21.   De Risi R, Goda K, Yasuda T, Mori N. Is flow velocity important in tsunami empirical fragility modeling?
636   *Earth-Science Reviews* 2017; **166**: 64–82.

637   22.   Ventura CE, Finn WDL, Onur T, Blanquera A, Rezai M. Regional seismic risk in British Columbia :
638   classification of buildings and development of damage probability functions. *Canadian Journal of Civil*
639   *Engineering* 2005; **32**(2): 372–387.

640   23.   Iervolino I, Giorgio M, Chioccarelli E. Markovian modeling of seismic damage accumulation. *Earthquake*
641   *Engineering & Structural Dynamics* 2016; **45**(3): 441–461.

642   24.   Goda K, Taylor CA. Effects of aftershocks on peak ductility demand due to strong ground motion records
643   from shallow crustal earthquakes. *Earthquake Engineering & Structural Dynamics* 2012; **41**(15): 2311–
644   2330.

645   25.   Goda K, Wenzel F, De Risi R. Empirical assessment of non-linear seismic demand of mainshock-aftershock
646   ground-motion sequences for Japanese earthquakes. *Frontiers in Built Environment* 2015; **1**: 6. DOI:
647   10.3389/fbuil.2015.00006.

648   26.   Halchuk S, Allen TI, Adams J, Rogers GC. Fifth generation seismic hazard model input files as proposed to
649   produce values for the 2015 National Building Code of Canada. *Geological Survey of Canada, Open File*
650   2014.

651   27.   Goda K, Atkinson GM. Seismic performance of wood-frame houses in south-western British Columbia.
652   *Earthquake Engineering & Structural Dynamics* 2011; **40**(8): 903–924.

653   28.   Jalayer F, De Risi R, Manfredi G. Bayesian Cloud Analysis: efficient structural fragility assessment using
654   linear regression. *Bulletin of Earthquake Engineering* 2015; **13**(4): 1183–1203.

655   29.   Lagaros ND, Fragiadakis M. Fragility assessment of steel frames using neural networks. *Earthquake Spectra*
656   2007; **23**(4): 735–752.

657   30.   White TW, Ventura CE. Seismic performance of wood-frame residential construction in British Columbia-
658   technical report. *Earthquake Eng. Research Facility Report No. 06-03,* University of British Columbia,
659   Vancouver, Canada, 2006.

660   31.   Folz B, Filiatrault A. Seismic analysis of woodframe structures. I: Model formulation. *Journal of Structural*
661   *Engineering* 2004; **130**(9): 1353–1360.

662   32.   Folz B, Filiatrault A. Seismic analysis of woodframe structures. II: Model implementation and verification.
663   *Journal of Structural Engineering* 2004; **130**(9): 1361–1370.

664   33.   Folz B, Filiatrault A. Cyclic analysis of wood shear walls. *Journal of Structural Engineering* 2001; **127**(4):
665   433–441.

666   34.   Pan Y, Ventura CE, Finn WDL. Effects of ground motion duration on the seismic performance and collapse
667   rate of light-frame wood houses. *Journal of Structural Engineering* 2018; **144**(8), 04018112-1.

668   35.   Ebrahimian H, Jalayer F, Lucchini A, Mollaioli F, Manfredi G. Preliminary ranking of alternative scalar and
669   vector intensity measures of ground shaking. *Bulletin of Earthquake Engineering* 2015; **13**(10): 2805–2840.

670   36.   Porter K, Scawthorn CR, Beck JL. Cost-effectiveness of stronger woodframe buildings. *Earthquake Spectra*
671   2006; **22**(1): 239–266.

672   37.   Charvet I, Ioannou I, Rossetto T, Suppasri A, Imamura F. Empirical fragility assessment of buildings
673   affected by the 2011 Great East Japan tsunami using improved statistical models. *Natural Hazards* 2014;
674   **73**(2): 951–973.

675   38.   Jalayer F, Beck JL, Zareian F. Analyzing the sufficiency of alternative scalar and vector intensity measures
676   of ground shaking based on information theory. *Journal of Engineering Mechanics* 2012; **138**(3): 307–316.

677   39.   Christovasilis IP, Filiatrault A, Constantinou MC, Wanitkorkul A. Incremental dynamic analysis of
678   woodframe buildings. *Earthquake Engineering & Structural Dynamics* 2009; **38**(4): 477–496.

679   40.   Mollaioli F, Lucchini A, Cheng Y, Monti G. Intensity measures for the seismic response prediction of base-
680   isolated buildings. *Bulletin of Earthquake Engineering* 2013; **11**(5): 1841–1866.

681   41.   Abrahamson N, Gregor N, Addo K. BC Hydro ground motion prediction equations for subduction
682   earthquakes. *Earthquake Spectra* 2016; **32**(1): 23–44.

683   42.   Ghofrani H, Atkinson GM. Ground-motion prediction equations for interface earthquakes of M7 to M9
684   based on empirical data from Japan. *Bulletin of Earthquake Engineering* 2014; **12**(2): 549–571.

685   43.   Christidis AA, Dimitroudi EG, Hatzigeorgiou GD, Beskos DE. Maximum seismic displacements evaluation

686   of steel frames from their post-earthquake residual deformation. *Bulletin of Earthquake Engineering* 2013;
687   **11**(6): 2233–2248.
688   44. Tesfamariam S, Goda K. Seismic performance evaluation framework considering maximum and residual
689   inter-story drift ratios: application to non-code conforming reinforced concrete buildings in Victoria, BC,
690   Canada. *Frontiers in Built Environment* 2015; **1**(18). DOI: 10.3389/fbuil.2015.00018.
691   45. Federal Emergency Management Agency (FEMA). Prestandard and commentary for the seismic
692   rehabilitation of buildings. *Report No. FEMA-356*, Washington, DC, 2000.
693   46. Nazari N, Van De Lindt JW, Li Y. Effect of mainshock-aftershock sequences on woodframe building
694   damage fragilities. *Journal of Performance of Constructed Facilities* 2013; **29**(1), 04014036-1.
695   47. Federal Emergency Management Agency (FEMA). Seismic performance assessment of buildings. *Report*
696   *No. FEMA P-58*, Washington, DC, 2014.
697   48. Rudolf J, Ventura CE, Prion H. Static and dynamic testing of shear wall panels for typical wood frame
698   residential construction in British Columbia, 1998.
699   49. Lallemant D, Kiremidjian A, Burton H. Statistical procedures for developing earthquake damage fragility
700   curves. *Earthquake Engineering & Structural Dynamics* 2015; **44**(9): 1373–1389.
701   50. Raghunandan M. Influence of long duration ground shaking on collapse of reinforced concrete structures,
702   *Ph.D. thesis*, Department of Civil, Environmental, and Architectural Engineering, University of Colorado,
703   2013.
704   51. Morell KD, Regalla C, Leonard LJ, Amos C, Levson V. Quaternary rupture of a crustal fault beneath
705   Victoria, British Columbia, Canada. *GSA Today* 2017; **27**. DOI: 10.1130/GSATG291A.1.
706   52. Boore DM, Stewart JP, Seyhan E, Atkinson GM. NGA-West2 equations for predicting PGA, PGV, and 5%
707   damped PSA for shallow crustal earthquakes. *Earthquake Spectra* 2014; **30**(3): 1057–1085.
708   53. Goda K. Assessment of Seismic Hazard and Risk, and Decision-Making under Uncertainty, *Ph.D. thesis*,
709   Department of Civil and Environmental Engineering, University of Western Ontario, 2007.
710   54. Zhang L, Werner MJ, Goda K. Spatiotemporal seismic hazard and risk assessment of aftershocks of M 9
711   megathrust earthquakes. *Bulletin of the Seismological Society of America* 2018; **108**(6): 3313–3335.
712   55. Luco N, Gerstenberger MC, Uma SR, Ryu H, Liel AB, Raghunandan M. A methodology for post-
713   mainshock probabilistic assessment of building collapse risk. *Ninth Pacific Conference on Earthquake*
714   *Engineering, Auckland, New Zealand*, 2011.
715